Linearized Relative Motion and Proximity Control of E-sail-based Displaced Orbits

Xiao Pan [a,†], **Alessandro A. Quarta** [b,‡], **Giovanni Mengali** [b,ζ], **Ming Xu** [a,ξ]

[a] School of Astronautics, Beihang University, Beijing 100191, China

[b] Dipartimento di Ingegneria Civile e Industriale, University of Pisa, I-56122 Pisa, Italy

Abstract: This paper discusses the linearized relative motion and control of Electric Solar Wind Sails (E-sails) operating in formation flight around a heliocentric displaced orbit. An E-sail is constituted by thin and centrifugally stretched tethers, and generates a propulsion by momentum interaction with the charged particles from the solar wind. Feasible regions and linear stability of circular displaced non-Keplerian orbits generated by E-sails are investigated using the latest thrust model. The linearized relative motion of E-sails in a formation flight is developed in the chief's orbital frame, and the linear stability of the relative motion is analysed with eigenvalue decomposition. Relative trajectories are classified into three categories, according to whether the relative orbit is stable, unstable or locally unstable, the latter corresponding to an instability in the along-track direction. Two control strategies are proposed for stabilization, the first one is an active control aiming to change the topology of the relative motion to eliminate the instability caused by positive real eigenvalues, and the other is a closed-loop feedback control to maintain stability in the along-track direction. Numerical simulations indicate a high accuracy of the linearized relative dynamical model and a good performance of the extra-control strategies.

Keywords: Electric Solar Wind Sail; displaced non-Keplerian orbit; formation flying; linear stability analysis

Nomenclature

a	=	propulsive acceleration vector [mm/s^2]
a_c	=	spacecraft characteristic acceleration [mm/s^2]

[†] Ph.D. Candidate, panxiao@buaa.edu.cn

[‡] Professor, a.quarta@ing.unipi.it

[ζ] Professor, g.mengali@ing.unipi.it

[ξ] Associate Professor, xuming@buaa.edu.cn

$\boldsymbol{n}$	=	normal unit vector
$\boldsymbol{r}$	=	Sun-spacecraft position vector [au]
$\boldsymbol{u}$	=	extra-control acceleration vector
z	=	displacement of the circular displaced orbit [au]
α	=	cone angle [deg]
α_n	=	pitch angle [deg]
$\Delta\boldsymbol{r}$	=	relative position from the deputy to the chief [au]
δn	=	azimuthal angle [deg]
η	=	eigenvalue
μ	=	Sun's gravitational parameter [km^3/s^2]
ρ	=	radius of the circular displaced orbit [au]
τ	=	switching parameter
ω	=	spacecraft angular velocity [deg/day]
ϖ	=	Keplerian orbit angular velocity [deg/day]

Subscripts

0	chief spacecraft
1	deputy spacecraft
$\oplus$	Earth
max	maximum

Superscripts

$\wedge$	unit vector

I. Introduction

The high cost of fuel required by spacecraft poses a great challenge to the development of space exploration activities. Motivated by it, many efforts have been devoted to the investigation of propellantless propulsion systems, which contribute to mitigate and even eliminate the constraint of mass consumption. Over the past years, some innovative propellantless propulsion systems have been proposed and attracted the interest of the scientific community. The photonic solar sail, which gains momentum by reflecting the light from the Sun [1], was the first propellantless propulsion system proposed and then analyzed from an engineering viewpoint [2]. In his excellent book, McInnes [3] provides a comprehensive and thorough investigation of solar sails in a number of possible mission applications, for

instance delivering payloads to high-energy orbits or planning sample return missions [4–7]. There exist also some other examples of propellantless propulsion systems, such as the magnetic sail [8-10] and the Mini-Magnetospheric Plasma Propulsion [11–13]. More recently, the Electric Solar Wind Sail (E-sail) concept has been introduced by Janhunen [14]. An E-sail is constituted by thin and centrifugally stretched tethers, charged by an on-board electron gun. The source of acceleration for an E-sail-based spacecraft is the momentum transported to the sail by the interaction of the artificial electric field generated by the tethers with the solar wind.

Because the E-sail thrust is inversely proportional to the Sun-spacecraft distance r, that is, decreases with the distance at a slower rate than that of a photonic solar sail (which instead scales as $1/r^2$) [15], an E-sail becomes a superior alternative in a number of mission scenarios, especially for those interplanetary transfers formulated within a time-optimal framework [16]. Most of the previous work about E-sail focused on its thrust model, with a continuous improvement in the accuracy and complexity of the mathematical models. In recent papers, Yamaguchi and Yamakawa [17] proposed a refined mathematical model, where the thrust modulus and the cone angle are written as functions of the E-sail attitude (characterized by the pitch angle, corresponding to the angle between the direction of the local solar wind and the normal to the E-sail nominal plane), through a sixth-order polynomial equation derived from numerical calculations. Later, Huo et al. [18] continued to improve the thrust model on this basis and provided an elegant analytical proof of the numerical results.

Based on the latest refined thrust model, this paper aims at studying the E-sail formation flying problem. There is a great deal of attention on formation flying of displaced orbits by photonic solar sails [19-21], but less attention is given to the cases in which the primary propulsion system is an E-sail. However, E-sails operating in close proximity, i.e., in a formation flight, can increase the reference propulsive acceleration of a single E-sail (the so-called characteristic acceleration) by disaggregating the payload [22] among multiple spacecraft. Moreover, a formation flying arrangement with multiple E-sails can improve the observation capability with higher resolution, which is of great importance for scientific missions such as the Mercury's magnetotail measurement [23] or the astronomical observation [24]. In this context, Wang et al. [25] have contributed to the study of E-sail formation around circular and elliptic displaced orbits. They used a set of displaced orbital elements to determine the formation boundaries, and designed a distributed coordinated control law that uses the information available from the neighbors to enable each vehicle to reach a final consensus [26]. Different from the methodology discussed in Ref. [25], this paper linearizes the relative motion of E-sails moving in a formation flight along a heliocentric, circular, displaced orbit, and provides a global view of their dynamics, linear stability, and control. Although the investigation process uses a classical

approach, the results of the relative motion of E-sails in close proximity are different from those related to solar sail-based spacecraft due to the different thrust models and the limitations on the thrust cone angle of an E-sail spacecraft.

The reminder of this paper is organized as follows. In section 2, circular displaced non-Keplerian orbits (DNKOs) maintained by E-sails are studied using their latest thrust model, with the aim of highlighting the feasible regions and their linear stability. Then, the linearized relative motion of E-sail formation flying is developed in Section 3. In the feasible region, the linear stability of the relative motions is analyzed to classify the relative trajectories into three cases, that is, stable relative orbits, unstable, and locally unstable orbits, the latter corresponding to orbits unstable in the along-track direction but stable in the other two directions. Next, two control strategies are proposed in Section 4 to stabilize the two kinds of unstable motions, where one is an active control that changes the topology of the relative motion to stabilize the unstable relative trajectories, and the other is a closed-loop feedback control that makes the along-track direction motion bounded. Finally, Section 5 is devoted to conclusions and future work.

II. E-sail-based Displaced Non-Keplerian Orbits

The mathematical thrust model of the electric solar wind sail underwent important revisions in last few years for obtaining a more accurate calculation of the propulsive acceleration vector [15-18, 27]. In this context, the latest E-sail thrust analytical model proposed in Ref. [18] is adopted in this paper.

Consider an E-sail-based spacecraft C, at a distance r from the Sun. Let P be the plane containing the E-sail tethers, and $\hat{\boldsymbol{n}}$ the unit vector orthogonal to P, pointing away from the Sun. Denote with $\boldsymbol{a}$ the propulsive acceleration vector, which belongs to the plane spanned by $\hat{\boldsymbol{n}}$ and $\boldsymbol{r}$. Note that the propulsive acceleration and the sail attitude are related to the pitch angle $\alpha_n \in [0, \pi/2]$ rad and the cone angle α, where the former is the angle between the direction of $\hat{\boldsymbol{n}}$ and that of the Sun-spacecraft vector $\boldsymbol{r}$, while the latter is the angle between $\boldsymbol{a}$ and $\boldsymbol{r}$.

Beside the pitch angle, the azimuthal angle δn is required for describing the E-sail attitude. To that end, let R be the local horizontal plane, which contains C and is orthogonal to $\boldsymbol{r}$, and ι be the fixed reference line obtained as the intersection of the orbital plane and the R plane, then δn is the angle between ι and the projection of $\hat{\boldsymbol{n}}$ onto R. The azimuthal angle of the propulsive acceleration $\boldsymbol{a}$ can be defined in a similar way.

According to the analytical model derived by Huo et al. [18], the expression of the E-sail propulsive acceleration $\boldsymbol{a}$ can be written in a compact, analytical, form as

$$\boldsymbol{a} = \tau \frac{a_c}{2} \left(\frac{r_\oplus}{r} \right) \left[\hat{\boldsymbol{r}} + (\hat{\boldsymbol{r}} \cdot \hat{\boldsymbol{n}}) \hat{\boldsymbol{n}} \right] \tag{1}$$

where τ is the switching parameter $\tau \in \{0, 1\}$, which models the fact that the E-sail thrust can be turned off ($\tau = 0$) at any time by simply switching off the on-board electron gun, $r_\oplus = 1$au is a reference distance, and a_c is the spacecraft

characteristic acceleration, defined as the maximum propulsive acceleration magnitude when $r = r_\oplus$. Note that the value of a_c depends on the geometry of the E-sail, such as the number of tethers, their length and voltage, as discussed in Ref. [18].
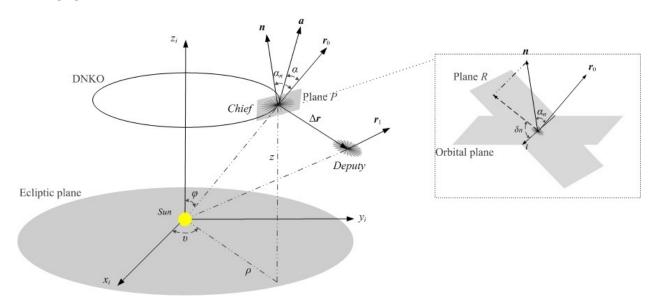

Fig.1 E-sail-based DNKO concept.

In particular, the propulsive acceleration magnitude $a \triangleq \|\boldsymbol{a}\|$ and the sail cone angle α can be written as functions of the sail pitch angle α_n as

$$a = \tau \frac{a_c}{2} \left(\frac{r_\oplus}{r} \right) \sqrt{1 + 3\cos^2 \alpha_n} \tag{2a}$$

$$\alpha = \arccos \left(\frac{1 + \cos^2 \alpha_n}{\sqrt{1 + 3\cos^2 \alpha_n}} \right). \tag{2b}$$

By solving the necessary condition $\partial\alpha/\partial\alpha_n = 0$, the maximum modulus of the cone angle α (referred to as α_{max}) and the corresponding value of the sail pitch angle α_n are calculated as follows

$$\alpha_{max} = 0.340 \text{ rad} , \qquad \alpha_n(\alpha_{max}) = 0.616 \text{ rad} . \tag{3}$$

The circular displaced orbits are characterized in terms of orbital period ω, orbital radius ρ and displacement z above the ecliptic. To maintain a circular orbit, the value of the required cone angle α and characteristic acceleration a_c are calculated with [28]

$$\alpha(\rho, z, \omega) = \arctan \left(\frac{(\omega/\varpi)^2 z}{\rho \left(1 + z^2/\rho^2 - (\omega/\varpi)^2 \right)} \right) \tag{4a}$$

$$a_c(\rho, z, \omega) = \frac{\mu}{r_\oplus} \frac{2}{r\sqrt{1 + 3\cos^2 \alpha_n}} \left(1 - \frac{\rho^2 (\omega/\varpi)^2}{\rho^2 + z^2} \right) \sqrt{1 + \frac{z^2}{\left[(\rho + z^2/\rho)/(\omega/\varpi)^2 - \rho \right]^2}} \tag{4b}$$

where $\varpi = \sqrt{\mu/r^3}$, and $r = \sqrt{\rho^2 + z^2}$ is the Sun-spacecraft (constant) distance. To summarize, the required value of

cone angle for a circular DNKO parameterized by (ρ, h, ω) can be obtained with Eq. (4a), while the corresponding values of E-sail pitch angle α_n are found by inverting Eq. (2b). When α_n is obtained, the characteristic acceleration a_c is calculated from Eq. (4b), while the value of propulsive acceleration modulus a is given by Eq. (2a).

We investigate now the feasibility and linear stability of the DNKOs with the latest E-sail thrust model. Following the methodology developed in Ref. [28], a final map of the admissible region for DNKOs (both feasible and stable) is obtained, and illustrated as the white region in Fig.2. The red curve represents the region boundary, characterized by $a_c<0$, the yellow curve denotes the region boundary with $\alpha>\alpha_{max}$, the green curves highlight the boundary of the linear unstable region. The red and yellow curves delimit the feasibility regions, while the green curves delimit the stability regions. From Fig.2, the feasible and stable region of DNKOs is relatively small, but lower the displacement is, the more possibilities of stability there are. Figure 2 provides a good reference for the design of E-sail based DNKO that are used for formation flying purposes discussed below.
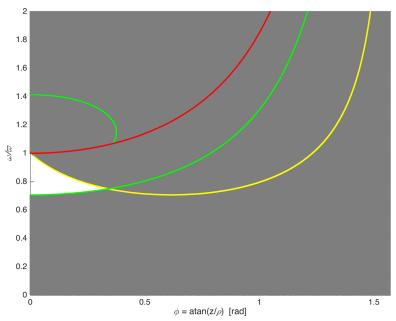

Fig.2 Feasible and stable region of DNKO (grey regions are unfeasible and/or unstable).

III. Linearized Relative Motion of Formation Flying

III.I. *Dynamical Model of Relative Motion*

In this section, the relative motion modelling between two spacecraft in heliocentric DNKO is analyzed. In particular, the E-sail-based spacecraft that tracks a circular displaced orbit is referred to as the chief, and the other is referred to as the deputy. Taking into account Eq. (1), the inertial (vectorial) equations of motion of both the chief and the deputy are given by

$$\ddot{\boldsymbol{r}}_0 = -\frac{\mu}{r_0^3}\boldsymbol{r}_0 + \frac{a_{c,0}}{2}\left(\frac{r_\oplus}{r_0}\right)\left[\hat{\boldsymbol{r}}_0 + \left(\hat{\boldsymbol{r}}_0 \cdot \boldsymbol{n}_0\right)\boldsymbol{n}_0\right] \tag{5a}$$

$$\ddot{\boldsymbol{r}}_1 = -\frac{\mu}{r_1^3}\boldsymbol{r}_1 + \frac{a_{c,1}}{2}\left(\frac{r_\oplus}{r_1}\right)\left[\hat{\boldsymbol{r}}_1 + \left(\hat{\boldsymbol{r}}_1 \cdot \boldsymbol{n}_1\right)\boldsymbol{n}_1\right] \tag{5b}$$

Let $\Delta\boldsymbol{r} = \boldsymbol{r}_1 - \boldsymbol{r}_0$ denote the (relative) position of the deputy with respect to the chief. Subtracting Eq. (5a) from (5.b) yields

$$
\begin{aligned}
\Delta\ddot{\boldsymbol{r}} =& -\frac{\mu}{\|\boldsymbol{r}_1 + \Delta\boldsymbol{r}\|^3}\left(\boldsymbol{r}_1 + \Delta\boldsymbol{r}\right) + \frac{\mu}{r_1^3}\left(\boldsymbol{r}_1 + \Delta\boldsymbol{r}\right) + \frac{a_{c,0}}{2}\left(\frac{r_\oplus}{\|\boldsymbol{r}_1 + \Delta\boldsymbol{r}\|^2}\right)\left(\boldsymbol{r}_1 + \Delta\boldsymbol{r}\right) - \frac{a_{c,1}}{2}\left(\frac{r_\oplus}{r_1^2}\right)\boldsymbol{r}_1 \\
&+ \frac{a_{c,0}}{2}\left(\frac{r_\oplus}{\|\boldsymbol{r}_1 + \Delta\boldsymbol{r}\|}\right)\cos\alpha_{n,0}\boldsymbol{n}_0 - \frac{a_{c,1}}{2}\left(\frac{r_\oplus}{r_1}\right)\cos\alpha_{n,1}\boldsymbol{n}_1
\end{aligned}
\tag{6}
$$

Introduce now the inertial reference frame ξ and the orbital reference frame ς [29], so that the relative acceleration in the chief's orbital reference frame ς can be written as

$$\Delta\ddot{\boldsymbol{r}} = \frac{d^{2\varsigma}\Delta\boldsymbol{r}}{dt^2} + 2\,^\xi\boldsymbol{\omega}^\varsigma \times \frac{d^\varsigma\Delta\boldsymbol{r}}{dt} + \frac{d\,^\xi\boldsymbol{\omega}^\varsigma}{dt}\times\Delta\boldsymbol{r} + \,^\xi\boldsymbol{\omega}^\varsigma \times\left(\,^\xi\boldsymbol{\omega}^\varsigma \times \Delta\boldsymbol{r}\right) \tag{7}$$

where $\,^\xi\boldsymbol{\omega}^\varsigma$ denotes the angular velocity vector of frame ς relative to frame ξ, given by

$$\,^\xi\boldsymbol{\omega}^\varsigma = \begin{bmatrix}\omega_0\cos\varphi_0 & 0 & \omega_0\sin\varphi_0\end{bmatrix}^T. \tag{8}$$

The chief position vector can be written as $\boldsymbol{r}_0 = \begin{bmatrix}r_0 & 0 & 0\end{bmatrix}^T$, and let $\{\Delta\boldsymbol{r}\}_\varsigma = \begin{bmatrix}x & y & z\end{bmatrix}^T$, so that the equations of relative motions in the orbit frame become

$$
\begin{aligned}
\ddot{x} - 2\omega\sin\varphi\,\dot{y} + \omega^2\left(\sin\varphi\cos\varphi z - \sin^2\varphi x\right) =& \frac{-\mu\left(r_0 + x\right)}{\left[\left(r_0 + x\right)^2 + y^2 + z^2\right]^{3/2}} + \frac{\mu}{r_0^2} + \frac{a_{c,1}r_\oplus}{2}\frac{\left(r_0 + x\right)}{\left(r_0 + x\right)^2 + y^2 + z^2} - \frac{a_{c,0}r_\oplus}{2}\frac{1}{r_0} \\
&+ \frac{a_{c,1}r_\oplus}{2}\frac{\cos\alpha_{n,1}n_{1,x}}{\sqrt{\left(r_0 + x\right)^2 + y^2 + z^2}} - \frac{a_{c,0}r_\oplus}{2}\frac{\cos\alpha_{n,0}n_{0,x}}{r_0}
\end{aligned}
$$

$$
\ddot{y} - 2\omega\left(-\sin\varphi\,\dot{x} + \cos\varphi\,\dot{z}\right) - \omega^2 y = \frac{-\mu y}{\left[\left(r_0 + x\right)^2 + y^2 + z^2\right]^{3/2}} + \frac{a_{c,1}r_\oplus}{2}\frac{y}{\left(r_0 + x\right)^2 + y^2 + z^2} + \frac{a_{c,1}r_\oplus}{2}\frac{\cos\alpha_{n,1}n_{1,y}}{\sqrt{\left(r_0 + x\right)^2 + y^2 + z^2}}
\tag{9}
$$

$$
\begin{aligned}
\ddot{z} + 2\omega\cos\varphi\,\dot{y} + \omega^2\left(\sin\varphi\cos\varphi x - \cos^2\varphi z\right) =& \frac{-\mu z}{\left[\left(r_0 + x\right)^2 + y^2 + z^2\right]^{3/2}} + \frac{a_{c,1}r_\oplus}{2}\frac{z}{\left(r_0 + x\right)^2 + y^2 + z^2} \\
&+ \frac{a_{c,1}r_\oplus}{2}\frac{\cos\alpha_{n,1}n_{1,z}}{\sqrt{\left(r_0 + x\right)^2 + y^2 + z^2}} - \frac{a_{c,0}r_\oplus}{2}\frac{\cos\alpha_{n,0}n_{0,z}}{r_0}
\end{aligned}
$$

where

$$\{\boldsymbol{n}_0\}_\varsigma = \begin{bmatrix}n_{0,x} \\ n_{0,y} \\ n_{0,z}\end{bmatrix} = \begin{bmatrix}\cos\alpha_{n,0} \\ 0 \\ \sin\alpha_{n,0}\end{bmatrix} \tag{10a}$$

$$\{\boldsymbol{n}_1\}_{\varsigma} = \begin{bmatrix} n_{1,x} \\ n_{1,y} \\ n_{1,z} \end{bmatrix} = \begin{bmatrix} \sin\varphi_1 \cos(\Delta\vartheta)\sin(\varphi_1 - \alpha_{n,1}) + \cos\varphi_1 \cos(\varphi_1 - \alpha_{n,1}) \\ \sin(\Delta\vartheta)\sin(\varphi_1 - \alpha_{n,1}) \\ -\cos\varphi_1 \cos(\Delta\vartheta)\sin(\varphi_1 - \alpha_{n,1}) + \sin\varphi_1 \cos(\varphi_1 - \alpha_{n,1}) \end{bmatrix}. \tag{10b}$$

To simplify Eq. (9), some parameters are specified, such as, for example, $\alpha_{n,1} = \alpha_{n,0}$ and $a_{c,1} = a_{c,0}$. It is reasonable to assume that the deputy has the same acceleration and thrust pitch angle as that of the chief, since they are close to each other at the initial time. As a result, the expressions of φ_1 and $\Delta\vartheta$ are

$$\varphi_1 = \arctan\left(\frac{\rho_0 + \rho}{z_0 + z}\right) = \arctan\left(\left(\tan\varphi_0 + \frac{x}{z_0}\sin\varphi_0 - \frac{z}{z_0}\cos\varphi_0\right)\left(\frac{1}{1 + z/z_0}\right)\right) \tag{11}$$

$$\Delta\vartheta = \vartheta_1 - \vartheta_0 = \frac{y}{\rho_0}. \tag{12}$$

The linearized dynamical model of the E-sail formation flying is given by

$$\Delta\ddot{\boldsymbol{r}} + \boldsymbol{A}\Delta\dot{\boldsymbol{r}} + \boldsymbol{B}\Delta\boldsymbol{r} = \boldsymbol{0} \tag{13}$$

where, omitting the subscript 0 in the symbols $\omega, \varPhi, a$, and α_n (since these are all parameters of the chief), we get

$$\boldsymbol{A} = 2\omega \begin{bmatrix} 0 & -\sin\varphi & 0 \\ \sin\varphi & 0 & -\cos\varphi \\ 0 & \cos\varphi & 0 \end{bmatrix}, \tag{14}$$

$$\boldsymbol{B} = \omega^2 \begin{bmatrix} -\sin^2\varphi & 0 & \sin\varphi\cos\varphi \\ 0 & -1 & 0 \\ \sin\varphi\cos\varphi & 0 & -\cos^2\varphi \end{bmatrix} + \frac{\mu}{r_0^3}\begin{bmatrix} -2 & 0 & 0 \\ 0 & 1 & 0 \\ 0 & 0 & 1 \end{bmatrix} - \frac{a}{2}\frac{r_\oplus}{r_0^2}\begin{bmatrix} -1 & 0 & 0 \\ 0 & 1 & 0 \\ 0 & 0 & 1 \end{bmatrix} - \frac{a}{2}\frac{r_\oplus \cos\alpha_n}{r_0^2\rho_0}\begin{bmatrix} -\rho_0\cos\alpha_n & 0 & 0 \\ 0 & r_0\sin(\varphi - \alpha_n) & 0 \\ -\rho_0\sin\alpha_n & 0 & 0 \end{bmatrix}$$

$$\tag{15}$$

The accuracy of the linearized dynamics is better appreciated with an example. The circular displaced orbit of the chief has a radius $\rho = 0.2 r_\oplus$, a displacement $z_0 = 0.004 r_\oplus$ and an angular velocity $\omega_0 = 0.76\varpi_0$. Assuming the initial conditions of the relative motion to be $[\Delta\boldsymbol{r}_0; \Delta\dot{\boldsymbol{r}}_0] = [10 \quad 10 \quad 100 \quad 0.01 \quad 0 \quad 0.01]^T$, the errors between the nonlinear and linearized relative orbits, integrated numerically for 5 years, are shown in Fig.3. During such a long mission time, the maximum error in the along-track direction is less than 0.12 km. Compared to the large spacecraft orbit, the accuracy of the linearized relative motions is acceptable. Because the relative orbit in this case is unstable and observing that in a stable case the error between the nonlinear and linearized relative dynamical models could be

further decreased, the linearized relative dynamics shows a relatively high performance in precision along the long-time mission.
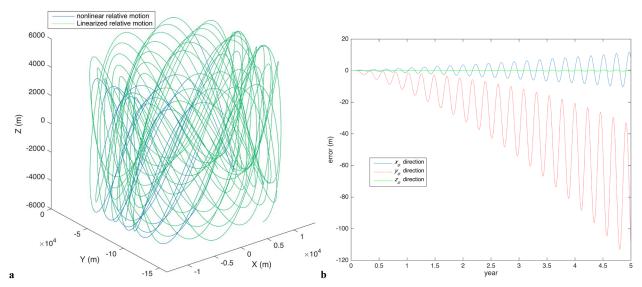

Fig.3 Error between the nonlinear and linearized relative dynamical models: a relative trajectory in the position space; b error in three coordinate components of the Chief's orbital frame.

III.II. *Linear Stability Analysis*

Based on the linearized Eq. (13), the linear stability of the relative motion can be studied by looking at the eigenvalues of the matrix M defined as

$$M = \begin{bmatrix} 0 & I \\ A & B \end{bmatrix}. \tag{16}$$

There are three pairs of eigenvalues, referred to as $\eta_{1,2}$, $\eta_{3,4}$ and $\eta_{5,6}$. Clearly, the eigenvalues vary when different parameters of the chief's orbit (φ, ω) are chosen. Below is a detailed analysis about their linear stability.

Firstly, due to the limitation on the maximum allowable modulus of the cone angle α, the feasible parameters of the displaced orbit are constrained. For a given radius ρ, the angle $\varphi = \arctan(\rho/z)$ depends on the displacement z, and using different values of the angular velocity ω, there are different feasible ranges for the displacement z. The feasible pairs (z, ω) are reassumed in Fig.4a, which shows that the DNKO with a smaller angular velocity has a wider feasible range of φ to design the displacement under a given radius ρ.

In the feasible region, the eigenvalues $\eta_{1,2}$, $\eta_{3,4}$ and $\eta_{5,6}$ are investigated when they cross the pairs (z, ω). It is found that $\eta_{1,2}$ is always a pair of zero eigenvalues, and $\eta_{5,6}$ is always a pair of conjugate imaginary eigenvalues, i.e., $\eta_{1,2} = 0$, $\eta_{5,6} = \pm\omega_3 i$ (with $\omega_3 > 0$). Differently, $\eta_{3,4}$ is more complicated, since it changes from a pair of conjugate imaginary to zero eigenvalues, and to real eigenvalues, when the displacement increases. The variations of $\eta_{3,4}$ and $\eta_{5,6}$ with displacement and angular velocity are plotted in Fig.4b and 4c. There are three possible

combinations of eigenvalues, that is, $[0, 0, \pm\omega_2 i, \pm\omega_3 i]$, $[0, 0, 0, 0, \pm\omega_3 i]$, or $[0, 0, \pm\lambda_2, \pm\omega_3 i]$, where $\omega_2 > 0$ and $\lambda_2 > 0$. The positive real eigenvalue $\eta_3 = +\lambda_2$ represents an instability of the relative motion, but the eigenvalue spectrum without real eigenvalues does not imply stability. In the cases of eigenvalue spectrum composed by zero eigenvalues, the stability depends on the initial value of the relative orbit. According to Fig.1 and Fig.4b, even though the DNKO with a lower angular velocity has a wider feasible range, the stable region of the formation flight is smaller than that with a relatively higher angular velocity.
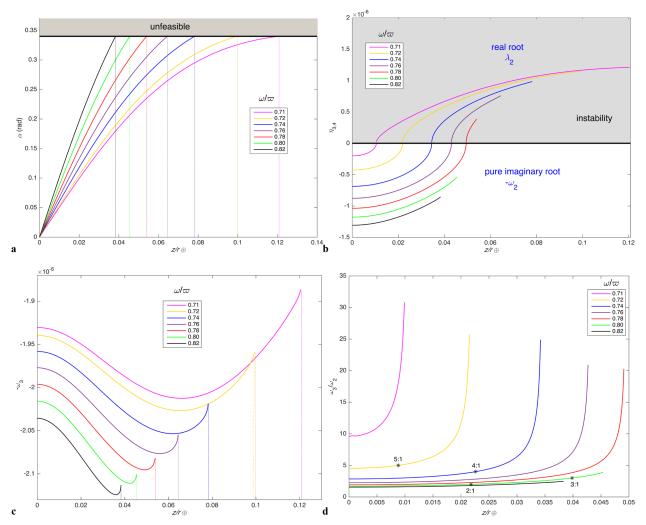

Fig.4 The variation of cone angle and eigenvalues with height and angular velocity: a feasible range of displacement with different ω, $\alpha_{max} = 0.34$ rad; **b** variation of $\eta_{3,4}$, changing from $\pm\omega_2 i$ to 0 to $\pm\lambda_2$; **c** variation of $\eta_{5,6}$, $\eta_{5,6} = \pm\omega_3 i$; **d** variation of ratio of ω_3/ω_2; $\rho = 0.2 r_\oplus$.

In particular, when the eigenvalue spectrum consists of 0, 0, $\pm\omega_2 i$, $\pm\omega_3 i$, where ω_2 and ω_3 are referred to as the natural frequencies, there exist some resonant orbits. Unlike the case of a solar sail in which the ratio ω_3/ω_2 increases from one to infinity [29], the ratio ω_3/ω_2 of relative motions with E-sails is different and limited, as shown in Fig.4d. The minimum ratio ω_3/ω_2, obtained by increasing the angular velocity, is limited by the feasibility condition, and its value is close to, but greater than 1. The maximum ratio ω_3/ω_2, instead, is limited by the stability constraint,

and its value is about 32. In some resonance cases in which $\omega_3/\omega_2 = m/n$ (with m and n positive commutative integers), the bounded relative orbit is periodic instead of quasi-periodic [29]. Thus, Fig.4d provides a good reference to design the periodic resonant relative orbits. Some examples are plotted in Fig.5, where all trajectories are propagated from $\left[\Delta \boldsymbol{r}_0 ; \Delta \dot{\boldsymbol{r}}_0\right] = [0; 0; 100; 0; 0; 0]^T$.

Fig.5 Periodic resonant relative orbits: **a** $\omega_3:\omega_2 = 2:1$; **b** $\omega_3:\omega_2 = 3:1$ **c** $\omega_3:\omega_2 = 4:1$ **d** $\omega_3:\omega_2 = 5:1$.

IV. Bounded Relative Trajectories by Extra-Control

The relative trajectories of E-sail-based spacecraft in a formation flying can be divided into three categories. The first ones, referred to as stable relative trajectories, are stable in all directions; the second ones, called locally unstable trajectories, are unstable in the along-track direction but stable in the other two directions; the third ones, referred to as fully unstable trajectories, are unstable in all directions. For different types of naturally unstable relative motions, we propose different control strategies, as is now discussed.

IV.I. Active Control for Fully Unstable Trajectories

According to the analysis of Ref. [30], an active control is regarded as a feasible and effective approach for the motion stabilization or maintenance, which is obtained by adjusting the E-sail grid voltage, and thus modifying the value of the spacecraft characteristic acceleration a_c.

Introducing the vector $X = \begin{bmatrix} r & \dot{r} \end{bmatrix}^T$, the controlled linearized equation of the system becomes

$$\dot{X} = MX + u_1 \tag{17}$$

where M is given by Eq. (16), and u_1 is the active control due to the grid voltage modulation (which is assumed to be sufficiently small) in the form

$$u_1 = -BK_1X, \quad B = \begin{bmatrix} 0 & 0 & 0 & 1 & 1 & 0 \end{bmatrix}^T, \quad K_1 = \begin{bmatrix} k_1 & 0 & 0 & 0 & 0 & 0 \end{bmatrix}, \tag{18}$$

where $k_1 \geq 0$ is the control (proportional) gain. The stability of the controlled system depends on the eigenvalues of the matrix $H_1 = M - BK_1$, and the eigenvalues of the matrix H_1 depend on the value of the control gain k_1.

As previously discussed, the relative orbit is fully unstable, due to the existence of a positive real eigenvalue $\eta_3 = +\lambda_2$, so that only by eliminating such an eigenvalue the relative trajectory may become stable. A correspondence between the pair of eigenvalues $\eta_{3,4}$ and the value of k_1 is shown in Fig. 6. For a given system (ρ, z, ω), there exists a minimum (or critical) gain k_1 that changes $\eta_{3,4}$ from $\pm\lambda_2$ into $\pm\omega_2 i$. As for the other two pairs of eigenvalues, the values of $\eta_{1,2}$ are unchanged, i.e., $\eta_{1,2} = 0$, while the values of $\eta_{5,6}$ slightly change when k_1 is increased, but are still imaginary, which makes no difference in terms of stability.
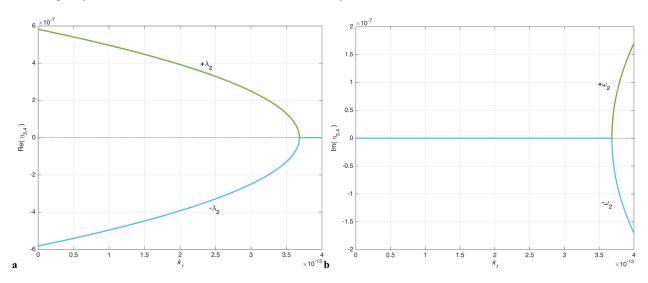

Fig.6 Relationship between the pair of eigenvalues $\eta_{3,4}$ and the value of k_1: $\rho = 0.2r_\oplus$, $z = 0.04r_\oplus$, $\omega = 0.72\varpi$; **a** variation of the real part of the eigenvalues $\eta_{3,4}$; **c** variation of the imaginary part of the eigenvalues $\eta_{3,4}$.

The active control is the first step to stabilize the relative motion, because there are still zero eigenvalues in the controlled system, in which the system stability depends on the initial values of the relative motions. Therefore, the active control can successfully transform the fully unstable trajectory into a stable or locally unstable one. As shown in Fig.4a and 4b, the system with a lower angular velocity has a wider feasible range of angle φ, but, at the same time, a wider unstable range caused by the positive real eigenvalues. An active control is therefore indispensable and contributes to enable the feasible range of stability, which extends the admissible region of E-sail-based formation. Fig.7 reports an example of the effects of the active control. In this simulation, $\rho = 0.2r_{\oplus}$, $z = 0.04r_{\oplus}$, $\omega = 0.72\varpi$, the initial values of the relative motion is $[\Delta r_0; \Delta \dot{r}_0] = [0;0;100;0;0;0]^T$, and the original eigenvalues of the system are $\eta_{1,2} = 0$, $\eta_{3,4} = \pm 5.8176 \cdot 10^{-7}$, $\eta_{5,6} = \pm 2.0008 \cdot 10^{-6} i$, which indicates a fully unstable motion. Using an active control with a gain $k_1 = 4 \cdot 10^{-13}$, the eigenvalues of the controlled system become $\eta_{1,2} = 0$, $\eta_{3,4} = \pm 1.701 \cdot 10^{-7} i$, $\eta_{5,6} = \pm 2.0089 \cdot 10^{-6} i$ and the relative trajectory is stable, as is shown in Fig.7.
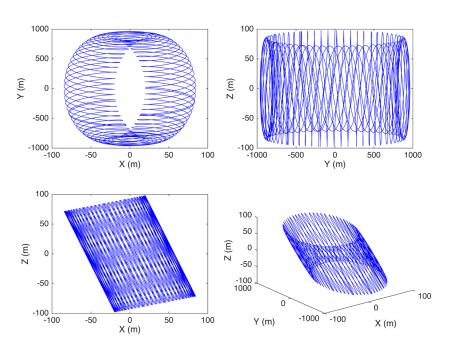

Fig.7 Stable relative trajectory by the active control: $\rho = 0.2r_{\oplus}$, $z = 0.04r_{\oplus}$, $\omega = 0.72\varpi$.

IV.II. *Feedback Control for Locally Unstable Relative Trajectory*

Since a slight deviation from the initial values generates an increase over time in the along-track component, a closed-loop control with only the feedback from Δy is proposed in this subsection as the second step to stabilize the locally unstable relative trajectory. The controller is constructed as

$$u_2 = BK_2X, \quad K_2 = \begin{bmatrix} 0 & k_2 & 0 & 0 & 0 & 0 \end{bmatrix} \tag{19}$$

where $k_2 \geq 0$ is a control gain.

For exemplary purposes, a comparison of the natural local unstable relative trajectory and the controlled one is plotted in Fig.8. In this simulation, $\rho = 0.2r_\oplus$, $z = 0.004r_\oplus$, $\omega = 0.76\varpi$, the initial values of the relative motion is $[\Delta \boldsymbol{r}_0; \Delta \dot{\boldsymbol{r}}_0] = [0;10;10;0;0;0]^T$, and the simulation time is 200 periods. As is indicated in Fig.8, with a feedback control applied in the along-track component in which $k_2 = 2 \cdot 10^{-16}$, the relative orbit can be bounded in a long mission time of about 20 years.
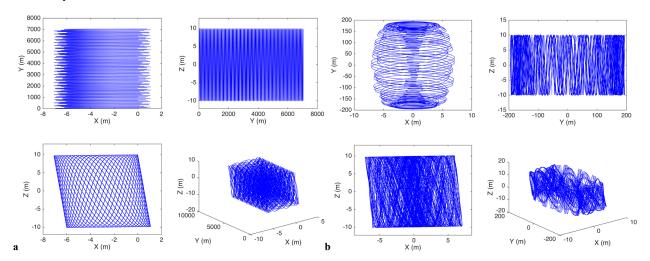

Fig.8 Comparison of the naturally and controlled local unstable relative trajectories: $\rho = 0.2r_\oplus$, $z = 0.004r_\oplus$, $\omega = 0.76\varpi$; **a** natural relative trajectory which is unstable in y-direction; **b** controlled relative trajecory which is bounded in all directions.

V. Conclusions

This paper has focused on the E-sail-based formation flying in (heliocentric) non-Keplerian displaced orbits. In particular, the paper proposes a global investigation about the maintenance of a circular displaced orbit, analyses the linearized dynamics of relative motion, and proposes a possible control strategy for stabilization. Starting from a refined thrust model of the E-sail propulsive acceleration vector, the linearized equations of relative dynamics are developed based on the requirements necessary for a displaced orbit maintenance. The linear stability of the relative motions is analyzed using the eigenvalue decomposition, where a positive real eigenvalue means an unstable relative motion, but zero eigenvalue means an uncertain stability, which also depends on the initial values. To deal with it, an active control is proposed to stabilize the unstable relative motion by changing the topology of the relative motion, and a closed-loop feedback control is proposed to make the along-track direction motion bounded. The simulation results indicate a high accuracy of the linearized relative dynamical model and a good performance of the extra-control strategies.

The natural extension of this work is to obtain an analytical solution of the linearized relative motions of E-sail-based spacecraft in a formation structure. Such a study may be accomplished, for example, by reducing the dynamical

models into a two-degrees-of-freedom system with the Routh reduction method.

Acknowledgments

Conflict of interest statement

The authors declared that they have no conflicts of interest to this work.

References

[1] L. Friedman, Starsailing: Solar Sails and Interstellar Travel, 1st edition, Science Editions, Wiley, ISBN 978-0471625933, 1988, Chaper. 1.

[2] J. Wright, Space Sailing, 1st edition, Routledge, ISBN 978-2881248429, 1992, pp. 93–121, Chaper. 4.

[3] C. R. McInnes, Solar sailing: technology, dynamics and mission applications, space science and technology, Springer-Verlag, Berlin, 1999.

[4] M. Xu, S. Xu, Nonlinear dynamical analysis for displaced orbits above a planet, Celestial Mechanics and Dynamical Astronomy 102 (4) (2008) 327–353, doi: 10.1007/s10569-008-9171-4.

[5] M. Ceriotti, C. R. McInnes, Generation of optimal trajectories for earth hybrid pole sitters, Journal of Guidance Control and Dynamics 34 (3) (2011) 847–859, doi: 10.2514/1.50935.

[6] J. Heiligers, M. Ceriotti, C. R. McInnes, et al, Displaced geostationary orbit design using hybrid sail propulsion, Journal of Guidance Control and Dynamics 34 (6) (2011) 1852–1866, doi: 10.2514/1.53807.

[7] J. Bookless, C. R. McInnes, Dynamics and control of displaced periodic orbits using solar-sail propulsion, Journal of Guidance, Control, and Dynamics 29 (3) (2006) 527–537, doi: 10.2514/1.15655.

[8] D. G. Andrews, R. M. Zubrin, Use of magnetic sails for mars exploration missions, in: AIAA/ASME/SAE/ASEE 25th Joint Propulsion Conference, Monterey (CA), 1989, paper AIAA 89-2861.

[9] R. M. Zubrin, D. G. Andrews, Magnetic sails and interplanetary travel, Journal of Spacecraft and Rockets 28 (2) (1991) 197–203, doi: 10.2514/3.26230.

[10] R. M. Zubrin, The use of magnetic sails to escape from low earth orbit, in: AIAA/SAE/ASME/ASEE 27th Joint Propulsion Conference, Sacramento (CA), 1991, paper AIAA 91-3352.

[11] R. M. Winglee, J. Slough, T. Ziemba, A. Goodson, Mini-magnetospheric plasma propulsion: tapping the energy of the solar wind for spacecraft propulsion, Journal of Geophysical Research 105 (A9) (2000) 21,067–21,077, doi: 10.1029/1999ja000334.

[12] G. Mengali, A. A. Quarta, Optimal missions with mini-magnetospheric plasma propulsion, Journal of Guidance, Control, and Dynamics 29 (1) (2006) 209–212, doi: 10.2514/1.18169.

[13] G. Mengali, A. A. Quarta, Mini-magnetospheric plasma propulsion for outer planet missions, Journal of Guidance, Control, and Dynamics 29 (5) (2006) 1239–1242, doi: 10.2514/1.21634.

[14] P. Janhunen, Electric sail for spacecraft propulsion, Journal of Propulsion and Power 20 (4) (2004) 763–764, doi: 10.2514/1.8580.

[15] A. Sanchez-Torres, Drag and propulsive forces in electric sails with negative polarity, Advances in Space Research 57 (4) (2016) 1065–1071, doi: 10.1016/j.asr.2015.12.013.

[16] A. A. Quarta, G. Mengali, Minimum-time trajectories of electric sail with advanced thrust model, Aerospace Science and Technology 55 (2016) 419-430, doi: 10.1016/j.ast.2016.06.020.

[17] K. Yamaguchi, H. Yamakawa, Study on orbital maneuvers for electric sail with on-off thrust control, Aerospace Technology Japan, the Japan Society for Aeronautical and Space Sciences 12 (2013) 79–88, doi: 10.2322/astj.12.79.

[18] M. Huo, G. Mengali, A. A. Quarta, Electric sail thrust model from a geometrical perspective, Journal of Guidance, Control, and Dynamics 41 (3) (2018) 734–740, doi: 10.2514/1.G003169.

[19] S. Gong, H. Baoyin, J. Li, Solar sail formation flying around displaced solar orbits, Journal of Guidance, Control, and Dynamics 30 (4) (2007) 1148–1152, doi: 10.2514/1.24315.

[20] S. Gong, H. Baoyin, J. Li, Relative orbit design and control of formation around displaced solar orbits, Aerospace Science and Technology 12 (2), (2008) 195–201, doi: 10.1016/j.ast.2007.05.004.

[21] X. Pan , M. Xu , H. Huang , et al, Bounded relative motions for formation flying in displaced orbits by low-thrust propulsion, Celestial Mechanics and Dynamical Astronomy 130 (7) (2018) 47, doi: 10.1007/s10569-018-9845-5.

[22] L. Mazal, P. Gurfil, Cluster flight algorithms for disaggregated satellites, Journal of Guidance, Control, and Dynamics 36 (1) (2013) 124–135, doi: 10.2514/1.57180.

[23] G. Aliasi, G. Mengali, A. A. Quarta, Special orbits for Mercury observation, Inner Solar System – Prospective Energy and Material Resources. Springer International Publishing 5 (2015) 101–126, doi: 10.1007/978-3-319-19569-8_5.

[24] F. Salazar, O. Winter, E. Macau, et al, Zero drift regions and control strategies to keep satellite in formation around triangular libration point in the restricted sun-earth-moon scenario, Advances in Space Research 56 (7) (2015) 1502–1518, doi: 10.1016/j.asr.2015.07.001.

[25] W. Wang, G. Mengali, A. A. Quarta, J. Yuan, Extreme values of relative distances for spacecraft in elliptic displaced orbits, Advances in Space Research 58 (2016) 475–487, doi: 10.1016/j.asr.2016.05.007.

[26] W. Wang, G. Mengali, A. A. Quarta, J. Yuan, Formation flying for electric sails in displaced orbits. part II: distributed coordinated control, Advances in Space Research 60 (2017) 1130–1147, doi: 10.1016/j.asr.2017.06.017.

[27] A. Sanchez-Torres, Propulsive force in an electric solar sail, Contributions to Plasma Physics 54 (3) (2014) 314–319, doi: 10.1002/ctpp.201410077.

[28] L. Niccolai, A. A. Quarta, G. Mengali, Electric sail-based displaced orbits with a refined thrust model, Proceedings of the Institution of Mechanical Engineers, Part G: Journal of Aerospace Engineering 232 (3) (2018) 423–432, doi: 10.1177/0954410016679195.

[29] X. Pan, M. Xu, Distributed situational observer in a displaced orbit: relative dynamics and control, Journal of Astronomical Telescopes, Instruments, and Systems 4 (4) (2018) 45001, doi: 10.1117/1.JATIS.4.4.045001.

[30] L. Niccolai, A. A. Quarta, G. Mengali, Electric sail active control law for artificial Lagrangian point maintenance, 11th IAA Symposium On The Future Of Space Exploration, Torino, Italy, June 17-19, 2019.